

Observation of Robust Néel Skyrmions in Metallic PtMnGa

Abhay K. Srivastava, Parul Devi, Ankit K. Sharma, Tianping Ma, Hakan Deniz, Holger L. Meyerheim, Claudia Felser, and Stuart S. P. Parkin*

Over the past decade the family of chiral noncollinear spin textures has continued to expand with the observation in metallic compounds of Bloch-like skyrmions in several B20 compounds, and antiskyrmions in a tetragonal inverse Heusler. Néel like skyrmions in bulk crystals with broken inversion symmetry have recently been seen in two distinct nonmetallic compounds, GaV₄S₈ and VOSe₂O₅ at low temperatures (below ≈13 K) only. Here, the first observation of bulk Néel skyrmions in a metallic compound PtMnGa and, moreover, at high temperatures up to ≈220 K is reported. Lorentz transmission electron microscopy reveals the chiral Néel character of the skyrmions. A strong variation is reported of the size of the skyrmions on the thickness of the lamella in which they are confined, varying by a factor of 7 as the thickness is varied from ≈90 nm to ≈4 μm. Moreover, the skyrmions are highly robust to in-plane magnetic fields and can be stabilized in a zero magnetic field using suitable field-cooling protocols over a very broad temperature range to as low as 5 K. These properties, together with the possibility of manipulating skyrmions in metallic PtMnGa via current induced spin-orbit torques, make them extremely exciting for future spintronic applications.

Today there is tremendous interest in chiral noncollinear spin textures that are typically stabilized by vector exchange interactions in non-centrosymmetric structures. Of these spin textures skyrmions and, more recently, antiskyrmions have been the focus of much attention.^[1] Although the latter, to date, have only been observed in a tetragonal inverse Heusler,^[2] skyrmions with a Bloch like character have been found in several metallic cubic B20 compounds^[3] and skyrmions with a bulk

type Néel structure have been found in two nonmetallic oxides,^[4] although only at very low temperatures. Here we report the first observation of bulk type Néel skyrmions in a metallic compound PtMnGa. Moreover, we directly image the skyrmions in thin lamellae using Lorentz transmission electron microscopy (ITEM). Of especial interest we find that the skyrmions can be stabilized over a wide range of temperature (5–220 K) and magnetic field, as compared to Bloch-skyrmions in B20 compounds. Furthermore, another important difference is that the size of the Néel skyrmions depends on the thickness of the PtMnGa lamella and increases monotonically with the thickness of the lamella. Finally, we show that skyrmions in PtMnGa are robust against large in-plane magnetic fields.

Single crystals of PtMnGa were prepared by conventional means (see the Supporting


Information) with sizes ranging up to 4 mm. These crystals are metallic (see the Supporting Information). The resistivity versus temperature curve shows a change in slope near ≈230 K that corresponds to the Curie temperature where PtMnGa undergoes a transition to a ferromagnetic state that is also clearly seen in magnetization versus temperature data (not shown). Several previous studies have reported models of the crystal structure of PtMnGa.^[5] In these, the atomic structure of PtMnGa was first categorized with a cubic C1_b structure with space group F43m^[5a,b] but later with a hexagonal Ni₂In-type structure.^[5c,d] In the latter case,^[5d] it was suggested that the Pt, Mn, and Ga atoms are located at Wyckoff sites 2c, 2a, and 2d in the space group P6₃/mmc (Nr.194). Both these structural types are centrosymmetric which is not consistent with our observation of skyrmions. Thus, we have carried out detailed studies to precisely determine the crystal structure of PtMnGa as we now discuss.

From both single-crystal X-ray diffraction (XRD) and high-angle annular dark-field scanning transmission electron microscopy (HAADF-STEM) we find that, although the PtMnGa structure bears a resemblance with the model discussed,^[5d] the actual structure clearly lacks inversion symmetry due to small but significant vertical relaxations of the Pt and Ga atoms along the [0001] direction. This lowers the space group symmetry from P6₃/mmc (Nr. 194) to the polar group P3m1 (Nr.156) and, thereby, fulfils the requirement of hosting Néel skyrmions in a non-centrosymmetric crystal structure with point group C_{3v}.^[6]

XRD experiments were carried out on bulk single crystals using Cu-K_{α1} radiation. Based on least squares refinement of

A. K. Srivastava, A. K. Sharma, T. Ma, Dr. H. Deniz, Dr. H. L. Meyerheim, Prof. S. S. P. Parkin
Max Planck Institute of Microstructure Physics
Weinberg 2, Halle (Saale) D-06120, Germany
E-mail: stuart.parkin@mpi-halle.mpg.de

A. K. Srivastava, A. K. Sharma, T. Ma, Prof. S. S. P. Parkin
Institute of Physics
Martin Luther University
Halle-Wittenberg, Halle (Saale) D-06120, Germany
Dr. P. Devi,^[†] Prof. C. Felser
Max Planck Institute for Chemical Physics of Solids
Nöthnitzer Straße 40, 01187 Dresden, Germany

 The ORCID identification number(s) for the author(s) of this article can be found under <https://doi.org/10.1002/adma.201904327>.

© 2019 The Authors. Published by WILEY-VCH Verlag GmbH & Co. KGaA, Weinheim. This is an open access article under the terms of the Creative Commons Attribution License, which permits use, distribution and reproduction in any medium, provided the original work is properly cited.

^[†]Present address: Ames Laboratory, Ames, IA, USA

DOI: 10.1002/adma.201904327

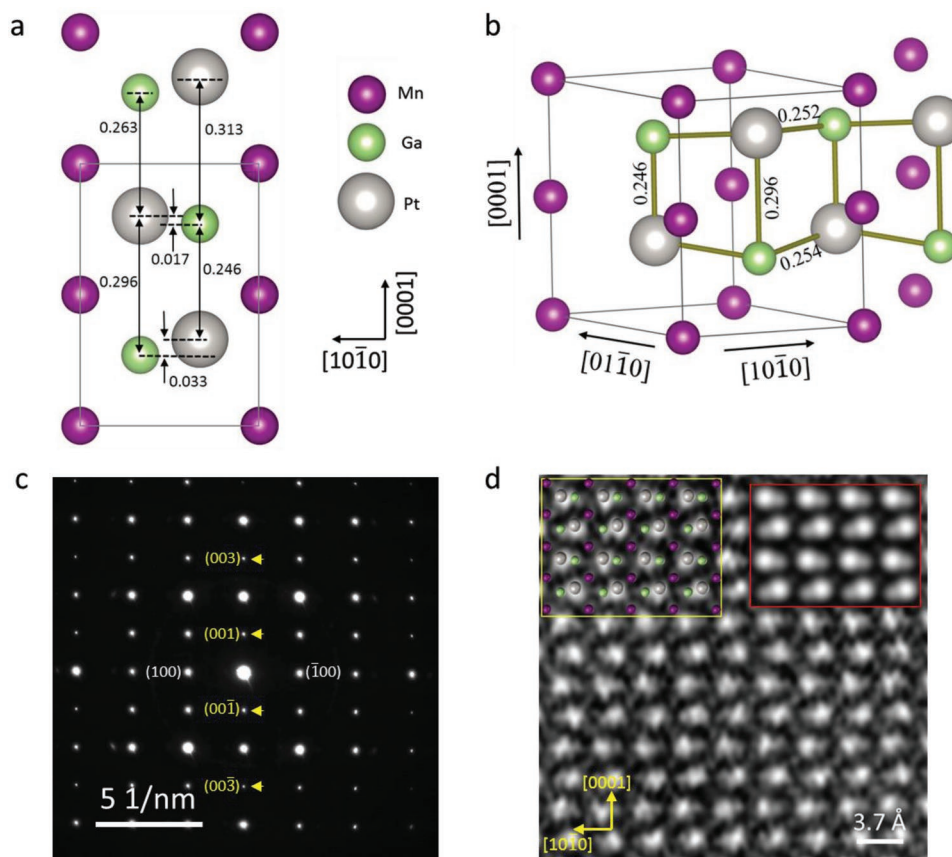


Figure 1. Structure of PtMnGa. a) XRD derived structure model. The unit cell is indicated by the solid lines. Distances along the [0001] directions are given in nanometers. b) Perspective view of the PtMnGa structure c) Selected-area electron diffraction pattern along [01 $\bar{1}$ 0] orientation of a PtMnGa lamella. The arrows indicate diffraction spots of the type (000*L*) with $L = 2n + 1$ ($n \in \mathbb{Z}$). d) Experimental HAADF-STEM image showing the atomic arrangements along [01 $\bar{1}$ 0]. Simulated STEM image (red rectangle) and approximate fitting of atoms (yellow rectangle) is shown for comparison. These measurements were performed at room temperature.

17 symmetry independent reflections, the atomic structure was analyzed to high accuracy. **Figure 1a** shows the atomic arrangement viewed along the [01 $\bar{1}$ 0] direction. The most important characteristic of the structure is the vertical rumpling within the two Pt–Ga–Pt chains of magnitude 0.017 and 0.033 nm, respectively. A perspective view of the structure is shown in **Figure 1b**. The two Pt (color grey) and two Ga (color green) atoms per unit cell are no longer symmetrically related to each other (*c*-glide plane, 6_3 screw axis), due to a symmetry lowering from $P6_3/mmc$ to $P3m1$, i.e., the structure lacks inversion symmetry. Unambiguous and direct evidence for this conclusion comes from the appearance of reflections, which are forbidden in $P6_3/mmc$, but which are observed in our experiments, albeit with very weak intensity (see the Supporting Information).

Thin lamellae of PtMnGa were prepared from bulk single crystals using focused ion beam techniques (see the Supporting Information). Lamellae that were oriented with the [01 $\bar{1}$ 0] direction perpendicular to the plane of the lamella were used to determine atomic arrangements using electron diffraction patterns and HAADF-STEM. An experimental electron diffraction pattern obtained from such a lamella is shown in **Figure 1c**. Diffraction spots of the type (000*L*) (with $L = 2n + 1$, $n \in \mathbb{Z}$),

that are forbidden for group $P6_3/mmc$, can be seen (denoted by arrows). **Figure 1d** shows a magnified experimental HAADF-STEM image along the [01 $\bar{1}$ 0] crystal direction. Because of its higher atomic number, Pt atoms are more prominent than Mn and Ga atoms. Detailed analysis of this image shows that the spacing between two consecutive atomic rows is not equal. This means that the Pt and Ga atoms are not fixed to the Wyckoff sites 2*c* and 2*d* of a Ni_2In -type structure, but instead they are relaxed along the [0001] direction. This relaxation results in lowering the symmetry and making the structure non-centrosymmetric. A simulation of the STEM image based on the structure proposed by XRD is shown (red rectangle) for comparison. It can be seen that the proposed structure fits well with the experimental observations. The yellow rectangle shows an approximate fitting of the atoms onto the STEM image. A detailed analysis of the experimental and simulated STEM images are given in the Supporting Information text and **Figures S1 and S2** in the Supporting Information. A simulation of the electron diffraction patterns and STEM image for group $P6_3/mmc$ is also shown for comparison. These experimental observations confirm that the structure is non-centrosymmetric C_{3v} rather than centrosymmetric Ni_2In -type structure reported in previous studies.

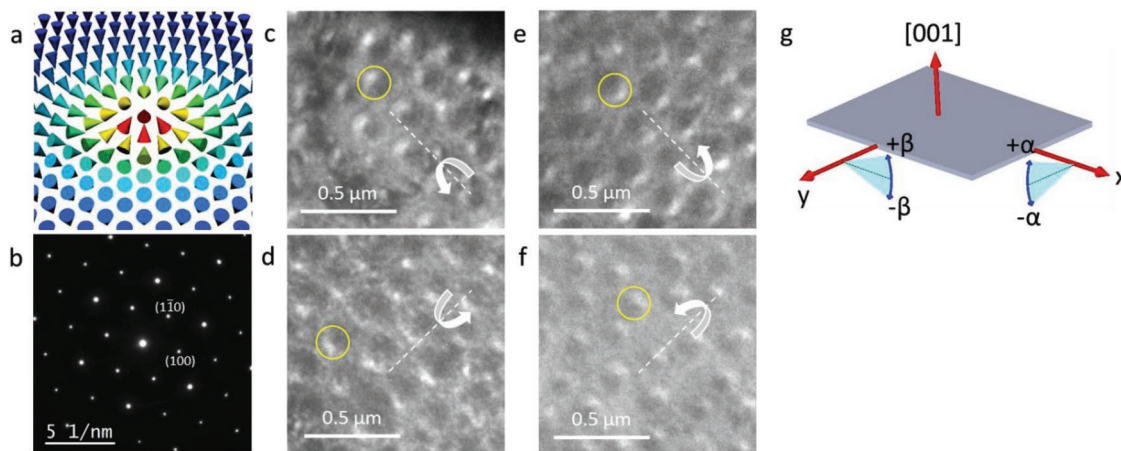


Figure 2. Observation of Néel skyrmions by LTEM. a) Spin texture of a Néel skyrmion. b) Selected-area electron diffraction pattern obtained at room temperature from a [0001] oriented lamella. c–f) Under-focused (1.5 nm) LTEM images recorded at 100 K with tilt angle as follows: c) $\alpha = -9^\circ$, d) $\beta = -19^\circ$, e) $\alpha = +9^\circ$, and f) $\beta = +16^\circ$. These images were recorded under a perpendicular applied field of 0.28 T. The dashed white lines in (c), (d), (e), and (f) represent the tilt axis, curved arrows represent the tilting direction and yellow circles identify a single skyrmion. g) Schematic representation of sample tilting along the x- and y-axes defining positive and negative α and β tilt angles.

LTEM has widely been used in skyrmion related studies due to its high spatial resolution and ability to distinguish various kinds of magnetic topological structures.^[2,3c,7] For a Néel-type skyrmion shown in **Figure 2a**, where the in-plane component of magnetization is either radially pointing out or pointing in, the total deflection of electrons is always compensated when the electron beam is perpendicular to the sample and hence results in no Lorentz contrast. However, when the sample is tilted, the projection of magnetization around the tilt axis causes an asymmetric deflection of electrons and thereby generates Lorentz contrast.^[7,8] This contrast is composed of half bright and half dark regions and depends on the sign and degree of tilting.^[7,9] Reversing the sign of the sample tilt reverses the contrast. Simulated LTEM images of a Néel skyrmion under different tilting condition are shown in Figure S3 in the Supporting Information.

Thin lamellae, oriented along [0001], were prepared from bulk single crystals using focused ion beam milling (see the Supporting Information), whose thickness was varied from ≈ 90 nm to ≈ 4 μm . Both uniform thickness lamella and wedges were prepared. Figure 2b shows the electron diffraction pattern obtained from a lamella of uniform thickness ≈ 265 nm showing that it is [0001] oriented. The sample was tilted away from the easy axis to generate Lorentz contrast. Tilting the sample along different directions results in changes in the contrast of Néel skyrmions, as mentioned previously. Figure 2c–f shows an alternation from bright to dark contrast of the skyrmions while tilting the sample from $-\alpha$ to $+\alpha$ (along x) or from $-\beta$ to $+\beta$ (along y). A schematic explanation of this sample tilting is shown in Figure 2g. A similar LTEM contrast has been previously observed for a “biskyrmion”^[10] and type-II bubbles.^[11] However, contrast for these spin-textures is found even without any tilt. Thus our observed spin structure is not consistent with a bubble or a Bloch skyrmion.

Detailed temperature and field-dependent LTEM measurements were carried out. We observe both thermodynamically stable Néel skyrmions over a limited temperature region and

metastable Néel skyrmions over a much wider temperature region. The observation of thermodynamically stable Néel skyrmions using LTEM is difficult for the following two main reasons: (i) the magnetic contrast of the sample decreases when approaching magnetic transition temperature ($T_c \approx 225$ K) and in increasing magnetic field, and (ii) the Néel skyrmion generates no contrast without tilting, as mentioned before. Although the sample can be tilted, small tilting does not provide observable contrast and large tilting in zero field with the subsequent application of field will result in an increased in-plane component of the magnetic field which increases the stability of the skyrmions.^[9] Therefore, to observe thermodynamically stable skyrmions, the field was applied along the [0001] direction and then the sample was tilted $\approx 24^\circ$ (high tilting value of 24° was used to obtain better contrast at 220 K). This procedure was done for several different temperatures from 200 to 225 K. At 200 K, no skyrmions were observed and above 220 K we could not observe any LTEM contrast. This means that thermodynamically stable skyrmions exist from ≈ 210 to ≈ 220 K. Figure S5 in the Supporting Information shows such skyrmions at 220 K with poor contrast. This shows that Néel skyrmions in this material are stable in a temperature–magnetic field (T – B) window close to T_c regardless of the field–temperature history. In this T – B window, we find that skyrmions are thermodynamically stable wherein a cycloidal state that is thermodynamically stable in zero magnetic field transforms into Néel skyrmions and then to the field polarized state by applying an increasing magnetic field. Images of the cycloidal phase are shown in Figure S5 in the Supporting Information.

At and below 200 K, a cycloidal state is observed throughout the sample when tilted 10° from the [0001] pole (lower tilting values were used at temperatures below 210 K for all other measurements to avoid stabilization caused by tilting). The absence of contrast in zero tilt establishes their Néel-like cycloidal nature wherein the spins rotate in a plane parallel to the cycloid propagation direction. Video S1 in the Supporting Information shows the contrast generation of such a cycloid

state when the sample is tilted away from the pole. With increasing field the cycloidal state simply transforms to a field polarized state and no skyrmions are observed during this process.

To stabilize Néel skyrmions in a broader temperature and field window, the sample was field cooled from above T_c (from 300 K) with an applied field of 0.096 T along [0001]. A similar field cooling mechanism has previously been used to obtain metastable Bloch-like skyrmions with field cooling.^[12] Néel skyrmions in our system are found to be stable even at zero field after the field cooling process. A small increase in size is observed after field removal. **Figure 3a** shows closely packed skyrmions at 150 K after removal of the external field. As compared to **Figure 2c–f**, an additional contrast can be seen within the skyrmion interior. This is clearly seen in the intensity line profile across one of the skyrmions, as shown in the inset to **Figure 3a**. This additional contrast shows that there is a uniformly magnetized core (pointing in $-z$) of the skyrmion that is well separated from the outside (pointing in $+z$) by the domain wall boundary. The core is increased in size compared to **Figure 2c–f** due to the lower magnetic field (here zero) so that it is big enough to be resolved by LTEM. **Figure S4** in the Supporting Information shows a simulated LTEM contrast and intensity profile of two skyrmions with different diameters. With an increase in the out of plane field, the core region shrinks and the skyrmion size decreases which is evident from **Figure 3b** and the line profile shown in the inset. For small sized skyrmions it was not possible to resolve the core from the domain wall and therefore these may be considered as skyrmions in which the magnetization direction changes continuously from the centre to the periphery of the skyrmion. A further increase in field results in a field polarized state.

The field and temperature dependence of the skyrmion size was studied in detail. **Figure 3c** shows the measured variation in skyrmion size with magnetic field at different temperatures for a lamella of uniform thickness (≈ 265 nm). For these measurements, the sample was tilted 10° from the pole. Some variation in the skyrmion size is found well above our LTEM resolution, as can be seen from **Figure 3a**, where the average value of the skyrmion diameter and the standard deviation in the size distribution is shown. As the magnetic field is increased the skyrmion sizes become more uniform. A large variation in skyrmion diameter occurs due to quenching of the spin structures after the field cooling process and local interactions between the skyrmions.^[10a,13] The average skyrmion size is found to decrease with increasing temperature and magnetic field. Above 210 K, the decreased magnetic contrast makes it impossible to obtain good LTEM contrast under the same tilting conditions.

Experiments were also performed on wedged samples to study the thickness dependence of the skyrmion phase stability. The dependence of Néel skyrmion size was studied as a function of lamella thickness, using two wedged lamellae W1 and W2 with thicknesses ranging from ≈ 90 to ≈ 260 nm and

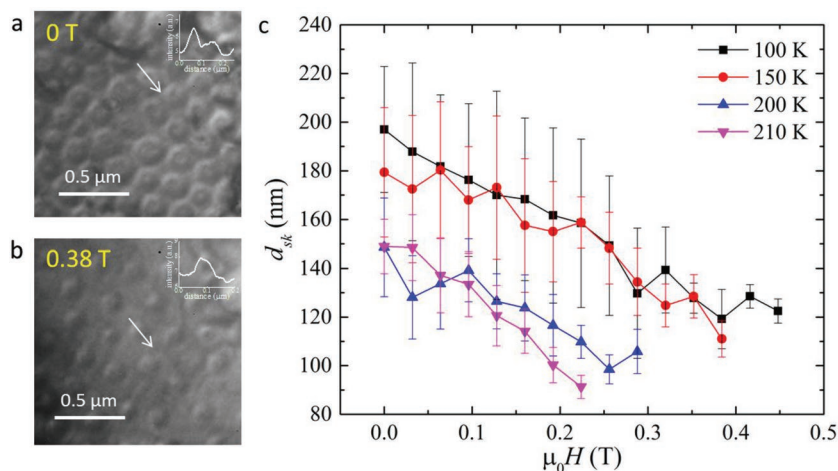


Figure 3. Skyrmion size as a function of magnetic field. a,b) Under-focused (1.2 mm) LTEM images recorded at 0 T (a) and 0.38 T (b) after field cooling in a perpendicular field of 0.096 T. Insets of (a) and (b) show intensity profiles along the direction of the white arrows shown in the figures. These images were taken at 150 K. c) Variation of skyrmion diameter as a function of magnetic field at different temperatures for a sample of uniform thickness (≈ 265 nm).

≈ 200 to ≈ 4000 nm, respectively. Lamella W1 was investigated using LTEM. **Figure S6** in the Supporting Information shows an overview image of the lamella W1 and its thickness profile as determined from electron energy loss spectroscopy (EELS). Without field cooling, cycloid spin spirals are observed and their thickness dependence can be seen in **Figure S7a** in the Supporting Information. The diameter of these spin spirals increases with thickness. The dependence of the cycloid on external magnetic field at 100 K is shown in **Figure S7** in the Supporting Information.

Skyrmions in the wedge lamella W1 were stabilized using the same field cooling process as mentioned before. The average skyrmion size is found to increase with lamella thickness. Three different regions of the wedge lamella A, B, and C (see **Figure S6a** in the Supporting Information) were chosen to measure the skyrmion size. The variation of average skyrmion size with thickness for these three regions are plotted and shown in **Figure S6b** in the Supporting Information. It is important to note that for low thickness, where the size of skyrmion is very small, it was not possible to distinguish the core region. However, as the lamella thickness increases, the skyrmion size also increases showing the core. With increasing field, the skyrmion core becomes smaller and smaller until it is difficult to resolve. This behavior is similar to that we discussed previously for uniform thickness lamellae.

In order to study the magnetic structure at thicknesses beyond those measurable by LTEM, we performed magnetic force microscopy (MFM) measurements on W2. In contrast to LTEM, the out-of-plane component of the magnetization is directly imaged and therefore the chirality of any nano-objects cannot be determined. However, we find that the MFM images obtained using the same protocols as used for LTEM are consistent with chiral Néel skyrmions which have the same size for the same thickness lamella. Thus, in the following we describe these objects observed in the MFM images as Néel skyrmions.

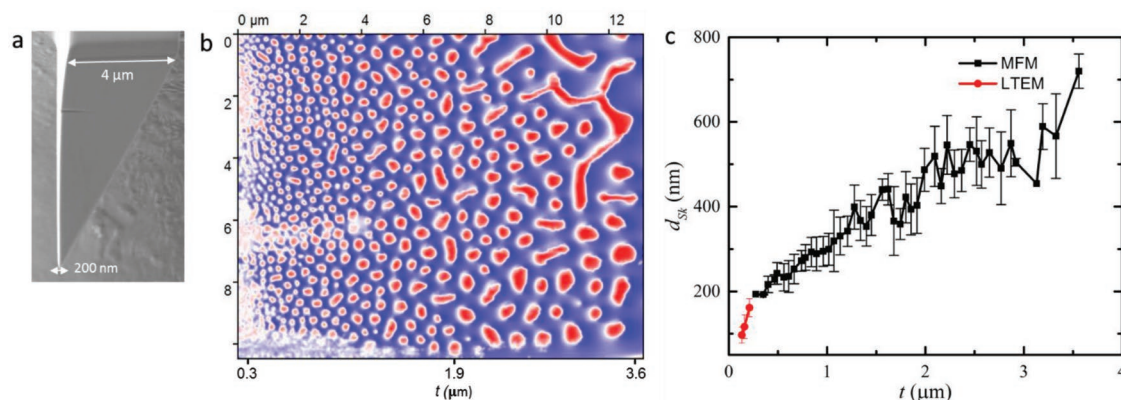


Figure 4. MFM images of Néel skyrmions. a) SEM side view of the wedge-shaped lamella. b) MFM image of Néel skyrmions in wedge W2 in 0.096 T at 100 K. c) Skyrmion diameter as a function of thickness (t) including both MFM and LTEM data.

A scanning electron microscopy image of the lamella W2 is shown in **Figure 4a**. Typical MFM data are summarized in **Figure 4b** after cooling W2 from 300 to 100 K in the presence of a magnetic field $H_{\perp} = 0.096$ T applied perpendicular to the wedge. A skyrmion phase is stabilized over the entire lamella. At large thicknesses the skyrmion phase is mixed with a few cycloids. Note that the direction of the cycloid is not tied to the underlying crystal structure (see **Figure S8d** in the Supporting Information) unlike for example, antiskyrmions.^[2] It is to be noted that the skyrmion size is not homogenous throughout the lamella thickness because of the field cooling process, which is discussed above in **Figure 3** description. However, the average skyrmion size is found to increase with increasing thickness. The average skyrmion size is estimated to be ≈ 190 nm for a thickness of ≈ 250 nm and ≈ 720 nm for a thickness of ≈ 3600 nm. The dependence of skyrmion size on the lamella thickness is summarized in **Figure 4c** and compared with the LTEM data for wedge W1. These data are in good agreement with each other and both sets of data show that there is a very strong dependence of the skyrmion size on lamella thickness. Effect of magnetic field on lamella W2 is shown in **Figure S8** in the Supporting Information.

Reports on Bloch skyrmions in chiral B20 systems, where the skyrmion size is determined by a competition between Heisenberg exchange and Dzyaloshinskii–Moriya Interaction (DMI), show that the skyrmion size is independent of sample

thickness.^[3c,14] However, biskyrmions and type-II bubbles, found in centrosymmetric systems, show a strong dependence on thickness.^[15] In these cases dipole–dipole interactions (DDI) play a very important role which, in general, can be ignored for B20 systems. Here the lower symmetry, that reflects the layered structure of PtMnGa, allows for strong contributions to the energy of the system in the case where the width of the boundary wall of the Néel skyrmion is small compared to the size of the magnetic object. In this case the Néel skyrmions have some “magnetic bubble” like character.^[16]

Since the Néel skyrmions in LTEM can only be observed when the sample is tilted and, consequently, there will always be an in-plane component of the applied field, we carried out studies to explore the stability of the Néel skyrmions in the presence of an in-plane magnetic field using MFM. A uniform lamella with ≈ 900 nm thickness was fabricated for this purpose. First, skyrmions were stabilized at 100 K after the same field cooling process as before and then the out-of-plane field was reduced to zero. Then a pure in-plane field was applied. Observations are shown in **Figure 5a–d**. Skyrmions are found to be stable even up to in-plane fields with large strengths of 1 T. There is a small decrease in contrast at these high in-plane fields.

In conclusion, we have found that PtMnGa has a non-centrosymmetric structure rather than the centrosymmetric structure reported in the literature. Although the structural

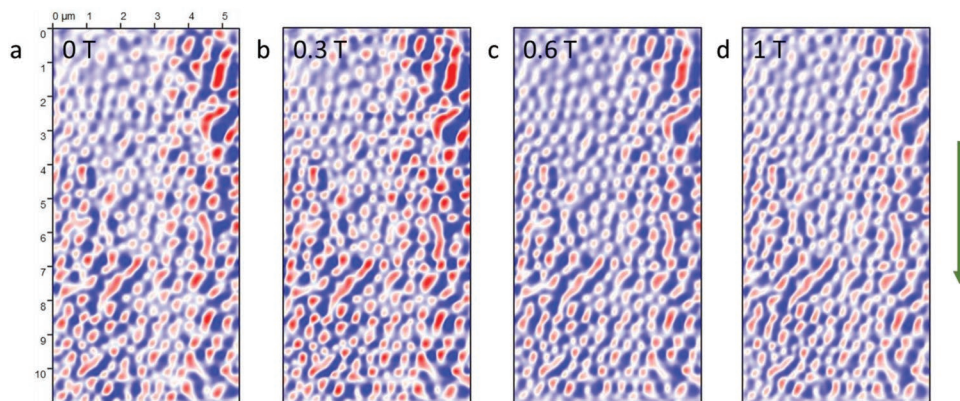


Figure 5. Effect of in-plane magnetic field. a–d) MFM images of metastable Néel skyrmions in a uniform lamella of thickness 900 nm in the presence of an in-plane magnetic field of strength: a) 0 T, b) 0.3 T, c) 0.6 T, and d) 1 T at 100 K. The arrow shows the direction of applied in-plane field.

differences are small, nevertheless, these are very important because they account for the observations that we make of robust Néel skyrmions in this system over a very wide range of temperature. These are the first observation of Néel skyrmions in a metallic system which make them highly interesting for applications in, for example, racetrack memories,^[17] in which Néel type noncollinear spin textures have been shown to be efficiently manipulated using chiral spin torques. Although we have not yet been able to manipulate the Néel skyrmions in these thick layer systems with current in the thick lamella we have used, we anticipate that for ultrathin layers this will be possible in the future. An important finding of our work is the very first observation of a significant dependence of Néel skyrmion size on thickness. Finally, we note that PtMnGa belongs to a large class of highly tunable magnetic metals whose properties can be readily tailored to optimize the skyrmionic properties to enable them to reach their full potential.

(Further details of the crystal structure investigation(s) may be obtained from the Fachinformationszentrum Karlsruhe, 76344 Eggenstein-Leopoldshafen (Germany), on quoting the depository number CSD-1938199)

Supporting Information

Supporting Information is available from the Wiley Online Library or from the author.

Acknowledgements

A.K.S., P.D., A.K.S., and T.M. contributed equally to this work. This project has received funding from the European Research Council (ERC) under the European Union's Horizon 2020 research and innovation program (Grant agreement No 670166) and the Deutsche Forschungsgemeinschaft (DFG, German Research Foundation)—Project number 403505322.

Conflict of Interest

The authors declare no conflict of interest.

Keywords

Lorentz transmission electron microscopy, non-centrosymmetric, skyrmions, spintronics

Received: July 7, 2019
Revised: November 3, 2019
Published online: December 26, 2019

- [1] a) M. Hoffmann, B. Zimmermann, G. P. Müller, D. Schürhoff, N. S. Kiselev, C. Melcher, S. Blügel, *Nat. Commun.* **2017**, *8*, 308; b) S. Huang, C. Zhou, G. Chen, H. Shen, A. K. Schmid, K. Liu, Y. Wu, *Phys. Rev. B* **2017**, *96*, 144412; c) W. Koshibae, N. Nagaosa, *Nat. Commun.* **2016**, *7*, 10542.
[2] A. K. Nayak, V. Kumar, T. Ma, P. Werner, E. Pippel, R. Sahoo, F. Damay, U. K. Rossler, C. Felser, S. S. P. Parkin, *Nature* **2017**, *548*, 561.

- [3] a) S. Mühlbauer, B. Binz, F. Jonietz, C. Pfleiderer, A. Rosch, A. Neubauer, R. Georgii, P. Boni, *Science* **2009**, *323*, 915; b) N. Kanazawa, Y. Onose, T. Arima, D. Okuyama, K. Ohoyama, S. Wakimoto, K. Kakurai, S. Ishiwata, Y. Tokura, *Phys. Rev. Lett.* **2011**, *106*, 156603; c) X. Z. Yu, N. Kanazawa, Y. Onose, K. Kimoto, W. Z. Zhang, S. Ishiwata, Y. Matsui, Y. Tokura, *Nat. Mater.* **2010**, *10*, 106.
[4] a) I. Kezsmarki, S. Bordacs, P. Milde, E. Neuber, L. M. Eng, J. S. White, H. M. Ronnow, C. D. Dewhurst, M. Mochizuki, K. Yanai, H. Nakamura, D. Ehlers, V. Tsurkan, A. Loidl, *Nat. Mater.* **2015**, *14*, 1116; b) T. Kurumaji, T. Nakajima, V. Ukleev, A. Feoktystov, T. H. Arima, K. Kakurai, Y. Tokura, *Phys. Rev. Lett.* **2017**, *119*, 237201.
[5] a) R. A. Dunlap, S. Jha, H. H. Seyoum, G. M. Julian, R. A. Pappas, J. W. Blue, *Hyperfine Interact.* **1983**, *16*, 689; b) F. A. Hames, J. Crangle, *J. Appl. Phys.* **1971**, *42*, 1336; c) K. H. J. Buschow, P. G. van Engen, *Phys. Status Solidi A* **1983**, *76*, 615; d) K. H. J. Buschow, D. B. De Mooij, *J. Less-Common Met.* **1984**, *99*, 125.
[6] a) A. Bogdanov, D. A. Yablonski, *J. Exp. Theor. Phys.* **1989**, *68*, 101; b) A. Bogdanov, A. Hubert, *J. Magn. Magn. Mater.* **1994**, *138*, 255.
[7] S. D. Pollard, J. A. Garlow, J. Yu, Z. Wang, Y. Zhu, H. Yang, *Nat. Commun.* **2017**, *8*, 14761.
[8] J. Cui, Y. Yao, X. Shen, Y. G. Wang, R. C. Yu, *J. Magn. Magn. Mater.* **2018**, *454*, 304.
[9] S. Zhang, J. Zhang, Y. Wen, E. M. Chudnovsky, X. Zhang, *Commun. Phys.* **2018**, *1*, 36.
[10] a) L. Peng, Y. Zhang, W. Wang, M. He, L. Li, B. Ding, J. Li, Y. Sun, X. G. Zhang, J. Cai, S. Wang, G. Wu, B. Shen, *Nano Lett.* **2017**, *17*, 7075; b) W. Wang, Y. Zhang, G. Xu, L. Peng, B. Ding, Y. Wang, Z. Hou, X. Zhang, X. Li, E. Liu, S. Wang, J. Cai, F. Wang, J. Li, F. Hu, G. Wu, B. Shen, X. X. Zhang, *Adv. Mater.* **2016**, *28*, 6887; c) X. Z. Yu, Y. Tokunaga, Y. Kaneko, W. Z. Zhang, K. Kimoto, Y. Matsui, Y. Taguchi, Y. Tokura, *Nat. Commun.* **2014**, *5*, 3198.
[11] a) J. C. Loudon, A. C. Twitchett-Harrison, D. Cortes-Ortuno, M. T. Birch, L. A. Turnbull, A. Stefancic, F. Y. Ogrin, E. O. Burgos-Parra, N. Bukin, A. Laurensen, H. Popescu, M. Beg, O. Hovorka, H. Fangohr, P. A. Midgley, G. Balakrishnan, P. D. Hatton, *Adv. Mater.* **2019**, *31*, e1806598; b) Y. Yao, B. Ding, J. Cui, X. Shen, Y. Wang, W. Wang, R. Yu, *Appl. Phys. Lett.* **2019**, *114*, 102404.
[12] a) K. Karube, J. S. White, N. Reynolds, J. L. Gavilano, H. Oike, A. Kikkawa, F. Kagawa, Y. Tokunaga, H. M. Rønnow, Y. Tokura, Y. Taguchi, *Nat. Mater.* **2016**, *15*, 1237; b) P. Milde, D. Köhler, J. Seidel, L. M. Eng, A. Bauer, A. Chacon, J. Kindervater, S. Mühlbauer, C. Pfleiderer, S. Buhbrandt, C. Schütte, A. Rosch, *Science* **2013**, *340*, 1076; c) H. Oike, A. Kikkawa, N. Kanazawa, Y. Taguchi, M. Kawasaki, Y. Tokura, F. Kagawa, *Nat. Phys.* **2015**, *12*, 62.
[13] a) S. Woo, K. Litzius, B. Krüger, M.-Y. Im, L. Caretta, K. Richter, M. Mann, A. Krone, R. M. Reeve, M. Weigand, P. Agrawal, I. Lemesch, M.-A. Mawass, P. Fischer, M. Kläui, G. S. D. Beach, *Nat. Mater.* **2016**, *15*, 501; b) K. Karube, J. S. White, D. Morikawa, M. Bartkowiak, A. Kikkawa, Y. Tokunaga, T. Arima, H. M. Rønnow, Y. Tokura, Y. Taguchi, *Phys. Rev. Mater.* **2017**, *1*, 074405.
[14] H. S. Park, X. Yu, S. Aizawa, T. Tanigaki, T. Akashi, Y. Takahashi, T. Matsuda, N. Kanazawa, Y. Onose, D. Shindo, A. Tonomura, Y. Tokura, *Nat. Nanotechnol.* **2014**, *9*, 337.
[15] a) H. Nakajima, H. Kawase, K. Kurushima, A. Kotani, T. Kimura, S. Mori, *Phys. Rev. B* **2017**, *96*, 024431; b) X. Z. Yu, Y. Tokunaga, Y. Kaneko, W. Z. Zhang, K. Kimoto, Y. Matsui, Y. Taguchi, Y. Tokura, *Nat. Commun.* **2014**, *5*, 3198.
[16] W. Jiang, P. Upadhyaya, W. Zhang, G. Yu, M. B. Jungfleisch, F. Y. Fradin, J. E. Pearson, Y. Tserkovnyak, K. L. Wang, O. Heinonen, S. G. te Velthuis, A. Hoffmann, *Science* **2015**, *349*, 283.
[17] S. S. P. Parkin, M. Hayashi, L. Thomas, *Science* **2008**, *320*, 190.